NASA/TM—2015-218446

Verification and Validation of a Three-Dimensional Generalized Composite Material Model

Canio Hoffarth, Joseph Harrington, and Subramaniam D. Rajan
Arizona State University, Tempe, Arizona

Robert K. Goldberg and Kelly S. Carney
Glenn Research Center, Cleveland, Ohio

Paul DuBois
George Mason University, Fairfax, Virginia

Gunther Blankenhorn
Livermore Software Technology Corporation, Livermore, California

January 2015

NASA STI Program . . . in Profile

Since its founding, NASA has been dedicated to the advancement of aeronautics and space science. The NASA Scientific and Technical Information (STI) program plays a key part in helping NASA maintain this important role.

The NASA STI Program operates under the auspices of the Agency Chief Information Officer. It collects, organizes, provides for archiving, and disseminates NASA's STI. The NASA STI program provides access to the NASA Aeronautics and Space Database and its public interface, the NASA Technical Reports Server, thus providing one of the largest collections of aeronautical and space science STI in the world. Results are published in both non-NASA channels and by NASA in the NASA STI Report Series, which includes the following report types:

- TECHNICAL PUBLICATION. Reports of completed research or a major significant phase of research that present the results of NASA programs and include extensive data or theoretical analysis. Includes compilations of significant scientific and technical data and information deemed to be of continuing reference value. NASA counterpart of peer-reviewed formal professional papers but has less stringent limitations on manuscript length and extent of graphic presentations.

- TECHNICAL MEMORANDUM. Scientific and technical findings that are preliminary or of specialized interest, e.g., quick release reports, working papers, and bibliographies that contain minimal annotation. Does not contain extensive analysis.

- CONTRACTOR REPORT. Scientific and technical findings by NASA-sponsored contractors and grantees.

- CONFERENCE PUBLICATION. Collected papers from scientific and technical conferences, symposia, seminars, or other meetings sponsored or cosponsored by NASA.

- SPECIAL PUBLICATION. Scientific, technical, or historical information from NASA programs, projects, and missions, often concerned with subjects having substantial public interest.

- TECHNICAL TRANSLATION. English-language translations of foreign scientific and technical material pertinent to NASA's mission.

Specialized services also include organizing and publishing research results, distributing specialized research announcements and feeds, providing information desk and personal search support, and enabling data exchange services.

For more information about the NASA STI program, see the following:

- Access the NASA STI program home page at *http://www.sti.nasa.gov*

- E-mail your question to *help@sti.nasa.gov*

- Phone the NASA STI Information Desk at 757-864-9658

- Write to:
  NASA STI Information Desk
  Mail Stop 148
  NASA Langley Research Center
  Hampton, VA 23681-2199

Verification and Validation of a Three-Dimensional Generalized Composite Material Model

Canio Hoffarth, Joseph Harrington, and Subramaniam D. Rajan
Arizona State University, Tempe, Arizona

Robert K. Goldberg and Kelly S. Carney
Glenn Research Center, Cleveland, Ohio

Paul DuBois
George Mason University, Fairfax, Virginia

Gunther Blankenhorn
Livermore Software Technology Corporation, Livermore, California

National Aeronautics and
Space Administration

Glenn Research Center
Cleveland, Ohio 44135

January 2015

Acknowledgments

Level of Review: This material has been technically reviewed by technical management.

Verification and Validation of a Three-Dimensional Generalized Composite Material Model

Canio Hoffarth, Joseph Harrington, and Subramaniam D. Rajan
Arizona State University
Tempe, Arizona 85004

Robert K. Goldberg and Kelly S. Carney
National Aeronautics and Space Administration
Glenn Research Center
Cleveland, Ohio 44135

Paul DuBois
George Mason University
Fairfax, Virginia 22030

Gunther Blankenhorn
Livermore Software Technology Corporation
Livermore, California 94551

Abstract

A general purpose orthotropic elasto-plastic computational constitutive material model has been developed to improve predictions of the response of composites subjected to high velocity impact. The three-dimensional orthotropic elasto-plastic composite material model is being implemented initially for solid elements in LS-DYNA as MAT213. In order to accurately represent the response of a composite, experimental stress-strain curves are utilized as input, allowing for a more general material model that can be used on a variety of composite applications. The theoretical details are discussed in a companion paper. This paper documents the implementation, verification and qualitative validation of the material model using the T800-F3900 fiber/resin composite material.

Introduction

Composite materials are now beginning to provide uses hitherto reserved for metals in structural systems such as airframes and engine containment systems, wraps for repair and rehabilitation and ballistic/blast mitigation systems. While material models exist that can be used to simulate the response of materials in these demanding structural systems, they are often designed for use with specific homogeneous materials such as metals (Refs. 1 and 2), polymers (Ref. 3) and wood (Ref. 4). While material models exist to simulate the impact response of composites, most are tailored specifically for a particular application and have limitations - purely elastic, no rate sensitivity, implementation for solid elements only, and limited damage and failure characterization (Refs. 5 to 10).

A few examples of different approaches to composite damage modeling include Littell et al. (Ref. 11), Matzenmiller et al. (Ref. 12), and others (Refs. 13 to 18). Yen's comprehensive model (Ref. 19) is implemented in LS-DYNA as *MAT_162. Availability of constitutive models for composite materials in LS-DYNA is discussed in some length in our companion paper (Ref. 20) and that explains the motivation for this study.

In the next section we briefly discuss the theoretical development of the constitutive model. This is followed by details of the numerical algorithm, verification tests for a composite used in the aerospace industry, the use of the composite in a high speed contact example and finally, concluding remarks including details of our ongoing and future work.

Orthotropic 3D Elasto-Plastic Composite Material Model

The material law that the model is built upon describes the elastic and permanent deformation of the composite with full three-dimensional implementation suitable for solid elements. Only the relevant equations used in the numerical algorithm are presented here. The theoretical basis and discussions are available in a companion paper (Ref. 20). Current development of the model includes the complete rate independent elasto-plastic deformation model, with damage and failure to be added later.

The commonly used Tsai-Wu composite failure model is generalized as a yield surface for the plasticity model and is defined as

$$f(\sigma) = a + \begin{pmatrix} F_1 & F_2 & F_3 & 0 & 0 & 0 \end{pmatrix} \begin{bmatrix} \sigma_{11} \\ \sigma_{22} \\ \sigma_{33} \\ \sigma_{12} \\ \sigma_{23} \\ \sigma_{31} \end{bmatrix} + \begin{bmatrix} \sigma_{11} \\ \sigma_{22} \\ \sigma_{33} \\ \sigma_{12} \\ \sigma_{23} \\ \sigma_{31} \end{bmatrix}^T \begin{bmatrix} F_{11} & F_{12} & F_{13} & 0 & 0 & 0 \\ F_{12} & F_{22} & F_{23} & 0 & 0 & 0 \\ F_{13} & F_{23} & F_{33} & 0 & 0 & 0 \\ 0 & 0 & 0 & F_{44} & 0 & 0 \\ 0 & 0 & 0 & 0 & F_{55} & 0 \\ 0 & 0 & 0 & 0 & 0 & F_{66} \end{bmatrix} \begin{bmatrix} \sigma_{11} \\ \sigma_{22} \\ \sigma_{33} \\ \sigma_{12} \\ \sigma_{23} \\ \sigma_{31} \end{bmatrix} \quad (1)$$

where $a = -1$ and

$$F_1 = \frac{1}{\sigma_{11}^T} - \frac{1}{\sigma_{11}^C} \qquad F_{11} = \frac{1}{\sigma_{11}^T \sigma_{11}^C} \qquad F_{44} = \frac{1}{\sigma_{12}^2}$$

$$F_2 = \frac{1}{\sigma_{22}^T} - \frac{1}{\sigma_{22}^C} \qquad F_{22} = \frac{1}{\sigma_{22}^T \sigma_{22}^C} \qquad F_{55} = \frac{1}{\sigma_{23}^2} \qquad (1a)$$

$$F_3 = \frac{1}{\sigma_{33}^T} - \frac{1}{\sigma_{33}^C} \qquad F_{33} = \frac{1}{\sigma_{33}^T \sigma_{33}^C} \qquad F_{66} = \frac{1}{\sigma_{31}^2}$$

$$F_{ij} = \frac{2}{\left(\sigma_{45}^{i-j}\right)^2} - \frac{F_i + F_j}{\sigma_{45}^{i-j}} - \frac{1}{2}(F_{ii} + F_{jj} + F_{kk}) \qquad i,j = 1,2,3, k = i+3$$

The stress components of the yield function coefficients correspond to the current yield stresses associated with a set of experimental stress-strain curves, which vary with the effective plastic strain, thus allowing the model to describe different hardening properties in each direction. The non-associative flow surface is defined as

$$h = \sqrt{H_{11}\sigma_{11}^2 + H_{22}\sigma_{22}^2 + H_{33}\sigma_{33}^2 + 2H_{12}\sigma_{11}\sigma_{22} + 2H_{23}\sigma_{22}\sigma_{33} + 2H_{31}\sigma_{33}\sigma_{11} + H_{44}\sigma_{12}^2 + H_{55}\sigma_{23}^2 + H_{66}\sigma_{31}^2} \quad (2)$$

where the H_{ij} terms are the constant flow rule coefficients. The rest of the details can be found in the companion paper (Ref. 20).

The first six flow rule coefficients are computed directly from the assumed flow rule coefficient value, H_{11} and the plastic Poisson's ratios.

$$H_{12} = -\nu_{12}^p H_{11} \qquad\qquad H_{23} = \frac{-\nu_{23}^p \nu_{12}^p}{\nu_{21}^p} H_{11}$$

$$H_{13} = -\nu_{13}^p H_{11}$$

$$H_{22} = \frac{\nu_{12}^p}{\nu_{21}^p} H_{11} \qquad\qquad H_{33} = \frac{\nu_{13}^p}{\nu_{31}^p} H_{11}$$

<div align="right">(3a)</div>

The last three flow rule coefficients (H_{44}, H_{55}, H_{66}) are calculated iteratively with the user-defined range to best fit the input experimental shear stress versus shear strain curves (Ref. 20). For example, to determine H_{44}, the following optimization problem is posed using the input curve for the "1-2" shear case.

Find H_{44} to minimize

$$f(H_{44}) = \sum_{i=1}^{n} \left[\left(\hat{\sigma}_{22} \right)_i - \left(\hat{\sigma}_{12} \right)_i \right]^2 \tag{3b}$$

such that

$$H_{44}^{\min} \le H_{44} \le H_{44}^{\max} \tag{3c}$$

where n is the number of data points on the master curve, $\left(\hat{\sigma}_{22} \right)_i$ is the ith effective stress value from the

master curve, and $\left(\hat{\sigma}_{12} \right)_i$ is the effective stress value for the shear curve using an assumed value of H_{44}.

Numerical Algorithm

In this initial implementation, we do not account for rate and temperature dependence, damage accumulation nor failure. The following experimental data are needed as LS-DYNA input.

(1) A total of 12 true stress versus true strain curves under quasi-static test conditions from (a) uniaxial tension in 1, 2 and 3-directions, (b) uniaxial compression in 1, 2 and 3-directions, (c) shear in 1-2, 2-3 and 3-1 planes and (d) off-axis (e.g., 45°) uniaxial tension or compression in 1-2, 2-3 and 3-1 planes. The tabulated x-y data for each curve is read in and used appropriately.
(2) The modulus of elasticity, Poisson's ratio and average plastic Poisson's ratio obtained from the tension and compression tests.

The effective plastic strain can be written in terms of the experimental stress versus total strain data. In the 1-direction for example, this is written as

$$\left. \begin{array}{l} \sigma_{11}^c \left(\varepsilon_{11}^p = \varepsilon_{11} - \dfrac{\sigma_{11}^c}{E_{11}} \right) \\[2mm] \varepsilon_e^p = \int \left(\sigma_{11} d\varepsilon_{11}^p / h \right) \end{array} \right\} \Rightarrow \sigma_{11}^c \left(\varepsilon_e^p \right) \tag{4}$$

where σ_{11}^c is the experimental compressive true stress in the 1-direction, ε_{11} is the total true strain in the 1-direction, E_{11} is the elastic modulus in the 1-direction, ε_{11}^p is the true plastic strain in the 1-direction,

ε_e^p is the effective plastic strain and h is the current value of the plastic potential function, which is equivalent to the effective stress, shown in Equation (2). The material model uses a typical elastic stress update as

$$\boldsymbol{\sigma}^{n+1} = \boldsymbol{\sigma}^n + \mathbf{C}\Delta t : \left(\dot{\boldsymbol{\varepsilon}} - \dot{\boldsymbol{\varepsilon}}^p \right) \tag{5}$$

where $\mathbf{C}$ is the orthotropic stiffness matrix, Δt is the time step, $\dot{\boldsymbol{\varepsilon}}$ is the total strain rate and $\dot{\boldsymbol{\varepsilon}}^p$ is the plastic strain rate. The stiffness matrix is written in terms of the compliance matrix as

$$\mathbf{C} = \mathbf{S}^{-1} = \begin{bmatrix} \dfrac{1}{E_{11}} & -\dfrac{v_{21}}{E_{22}} & -\dfrac{v_{31}}{E_{33}} & 0 & 0 & 0 \\ & \dfrac{1}{E_{22}} & -\dfrac{v_{32}}{E_{33}} & 0 & 0 & 0 \\ & & \dfrac{1}{E_{33}} & 0 & 0 & 0 \\ & & & \dfrac{1}{G_{12}} & 0 & 0 \\ & Sym & & & \dfrac{1}{G_{23}} & 0 \\ & & & & & \dfrac{1}{G_{31}} \end{bmatrix}^{-1} \tag{6}$$

where E_{ij} are the elastic moduli in the principal material directions, G_{ij} are the elastic shear moduli and v_{ij} are the elastic Poisson's ratios. The yield stresses used to determine the flow rule coefficients are summarized into a single vector, corresponding to each of the experimental test curves as $\mathbf{q}^T = \begin{bmatrix} \sigma_{11}^T & \sigma_{22}^T & \sigma_{33}^T & \sigma_{11}^C & \sigma_{22}^C & \sigma_{33}^C & \sigma_{12} & \sigma_{23} & \sigma_{31} & \sigma_{45-12}^C & \sigma_{45-23}^C & \sigma_{45-31}^C \end{bmatrix}$. Lastly, the consistency condition is written in terms of the rate of yield function as follows

$$\dot{f} = \frac{\partial f}{\partial \boldsymbol{\sigma}} \dot{\boldsymbol{\sigma}} + \frac{\partial f}{\partial \mathbf{q}} \dot{\mathbf{q}} = 0 \tag{7}$$

where the terms are as defined earlier. Equation (7) can be expanded as follows by introducing the elasto-plastic constitutive law

$$\dot{f} = \frac{\partial f}{\partial \boldsymbol{\sigma}} \left(\mathbf{C} : \dot{\boldsymbol{\varepsilon}} - \mathbf{C} : \dot{\lambda} \frac{\partial h}{\partial \boldsymbol{\sigma}} \right) + \frac{\partial f}{\partial \mathbf{q}} \dot{\lambda} \frac{d\mathbf{q}}{d\lambda} = 0 \tag{8}$$

where $\dot{\boldsymbol{\sigma}}$ is written in terms of the constitutive matrix and strain rates and λ is the effective plastic strain. Solving for the effective plastic strain rate produces the following equation.

$$\dot{\lambda} = \frac{\dfrac{\partial f}{\partial \boldsymbol{\sigma}} \mathbf{C} : \dot{\boldsymbol{\varepsilon}}}{\dfrac{\partial f}{\partial \boldsymbol{\sigma}} \mathbf{C} : \dfrac{\partial h}{\partial \boldsymbol{\sigma}} + \dfrac{\partial f}{\partial \mathbf{q}} \dfrac{d\mathbf{q}}{d\lambda}} \tag{9}$$

To numerically solve for the increment in effective plastic strain, a radial return algorithm is used. Initially, a perfectly elastic response is assumed. Thus, an elastic predictor is used to compute the stresses as

$$
\begin{aligned}
(\sigma_{11})^e &= (\sigma_{11})^n + C_{11}\Delta t(\dot{\varepsilon}_{11}) + C_{12}\Delta t(\dot{\varepsilon}_{22}) + C_{13}\Delta t(\dot{\varepsilon}_{33}) \\
(\sigma_{22})^e &= (\sigma_{22})^n + C_{12}\Delta t(\dot{\varepsilon}_{11}) + C_{22}\Delta t(\dot{\varepsilon}_{22}) + C_{23}\Delta t(\dot{\varepsilon}_{33}) \\
(\sigma_{33})^e &= (\sigma_{33})^n + C_{13}\Delta t(\dot{\varepsilon}_{11}) + C_{23}\Delta t(\dot{\varepsilon}_{22}) + C_{33}\Delta t(\dot{\varepsilon}_{33}) \\
(\sigma_{12})^e &= (\sigma_{12})^n + C_{44}\Delta t(\dot{\varepsilon}_{12}) \\
(\sigma_{23})^e &= (\sigma_{23})^n + C_{55}\Delta t(\dot{\varepsilon}_{23}) \\
(\sigma_{31})^e &= (\sigma_{31})^n + C_{66}\Delta t(\dot{\varepsilon}_{31})
\end{aligned}
\tag{10}
$$

With the elastic trial stresses computed, a trial yield function value can be calculated and used to determine if the load step is elastic or plastic. It should be noted that the elastic trial stress is used as the stress in the next step if the trial yield function value is less than or equal to zero. Otherwise, the stress state is beyond the yield surface and must be brought back using a radial return and plastic corrector, $\Delta\lambda$. If the trial yield function happens to be greater than zero, then $\Delta\lambda$ must be greater than zero. The value of $\Delta\lambda$ is determined using a secant iteration, with $\Delta\lambda^1 = 0$ for the first iteration and the second value for the increment of the plastic multiplier determined from consistency,

$$\Delta\lambda^2 = \frac{\left.\dfrac{\partial f}{\partial \boldsymbol{\sigma}}\right|_e : \left(\boldsymbol{\sigma}^e - \boldsymbol{\sigma}^n\right)}{\left.\dfrac{\partial f}{\partial \boldsymbol{\sigma}}\right|_e \mathbf{C} : \left.\dfrac{\partial h}{\partial \boldsymbol{\sigma}}\right|_e + \dfrac{\partial f}{\partial \mathbf{q}} \dfrac{d\mathbf{q}}{d\lambda}} \approx \frac{\left.\dfrac{\partial f}{\partial \boldsymbol{\sigma}}\right|_e : \left(\boldsymbol{\sigma}^e - \boldsymbol{\sigma}^n\right)}{\left.\dfrac{\partial f}{\partial \boldsymbol{\sigma}}\right|_e \mathbf{C} : \left.\dfrac{\partial h}{\partial \boldsymbol{\sigma}}\right|_e} \tag{11}$$

where the derivatives of $\mathbf{q}$ are taken as zero, meaning that the response is perfectly plastic. The initial calculation of the second increment corresponds to perfect plasticity in order to ensure that the stress state returns to the interior of the yield surface, resulting in a negative value of the yield function and bounding the solution. From each estimate of $\Delta\lambda$, the corresponding corrected stresses can be computed as well as the yield stresses obtained from the input stress versus effective plastic strain (λ) data. With these terms calculated for both estimates of $\Delta\lambda$, the yield function value for each can be computed with the third estimate evaluated as

$$\Delta\lambda^3 = \Delta\lambda^1 - f^1 \frac{\Delta\lambda^2 - \Delta\lambda^1}{f^2 - f^1} \tag{12}$$

The corrected stresses and yield stresses associated with $\Delta\lambda^3$ are then calculated and used to obtain a new estimate of the yield function value. Convergence of the secant iteration is determined by the following conditions, where f_3 is the value of the yield function given the effective plastic strain $\Delta\lambda^3$,

$$f_3 > 0 \Rightarrow \begin{cases} \Delta\lambda^1 = \Delta\lambda^3 \\ \Delta\lambda^2 = \Delta\lambda^2 \end{cases}; \quad f_3 < 0 \Rightarrow \begin{cases} \Delta\lambda^1 = \Delta\lambda^1 \\ \Delta\lambda^2 = \Delta\lambda^3 \end{cases}; \quad f_3 \approx 0 \Rightarrow \Delta\lambda = \Delta\lambda^3 \tag{13}$$

with the secant iteration continuing if the new yield function value is not less than some defined tolerance. Once convergence is met, the plastic multiplier increment to return the stress state to the yield surface is known and the stresses can be updated as

$$\boldsymbol{\sigma}^{n+1} = \boldsymbol{\sigma}^e - \mathbf{C} : \Delta\lambda \frac{\partial h}{\partial \boldsymbol{\sigma}}\bigg|_e \tag{14}$$

Finally, the yield stresses are updated as well, using the new value of the overall effective plastic strain, λ, in each input curve to determine the corresponding yield stress level as

$$q^{n+1} = q\left(\lambda^n + \Delta\lambda^3\right) \tag{15}$$

This results in anisotropic strain hardening, as a yield stress increase in each direction is initiated with plasticity in any direction, but at different levels. A detailed algorithm is presented below.

Step 1: Preprocessing
   (a) Convert stress/strain input curves to stress versus effective plastic strain using Equation (4).
   (b) Store initial yield stresses in $\mathbf{q}$.
   (c) Calculate and store the elastic moduli from the initial yield stress and strain values.
   (d) Store the three elastic Poisson's ratio values and flow rule coefficients from input.
   (e) Compute optimal values of the flow rule coefficients so as to match the input curves as closely as possible.

Step 2: Initialization
   Parameters available at start of step: $\mathbf{q}_n$, $\boldsymbol{\sigma}_n$, $(\dot{\boldsymbol{\varepsilon}}_n, \Delta t_n) \rightarrow \Delta\boldsymbol{\varepsilon}_n$, λ_n .

Step 3: Elastic predictor
   Compute and set the yield function coefficients using Equation (1a).
   Construct the constitutive matrix using Equation (6).
   Compute elastic trial stresses, $\boldsymbol{\sigma}^e_{n+1}$, using Equation (10).
   Compute the trial yield function, f^{trial}_{n+1} , using the elastic trial stresses in Equation (1).
   If $f^{trial}_{n+1} \leq 0$, the elastic solution is correct, set $\Delta\lambda_n = 0$ and go to stress update. Else go to plastic corrector.

Step 4: Plastic corrector
   Set $\Delta\lambda^1 = 0$.
   Calculate $\Delta\lambda^2$ from Equation (11).
   Loop through secant iteration for specified max number of iterations:

   Compute the new estimate of the stress for each plastic multiplier increment $\left(\Delta\lambda^1, \Delta\lambda^2\right)$ using

   Equation (14).

Calculate the effective plastic strains $\left(\lambda^1, \lambda^2\right)$ at the next time step using the estimates of the plastic multiplier increment; then obtain the strain hardening parameters with the effective plastic strain from the curve data (true stress as a function of effective plastic strain).

Compute new plastic multiplier increment, $\Delta\lambda^3$. Calculate new estimate for the yield function, f^3. If $\left|f^3\right| \leq tol$, set $\Delta\lambda = \Delta\lambda^3$, exit the loop and go to stress update. Else update secant iteration parameters using Equation (14) and go to next step of secant iteration.

Step 5: Stress Update

Calculate $\boldsymbol{\sigma}_{n+1}$ using Equation (14).

Step 6: Update history variables for plastic work and work hardening parameters ($\mathbf{q}$ and λ)

Set $\lambda_{n+1} = \lambda_n + \Delta\lambda_n$.

Determine new yield stresses, $\mathbf{q}_{n+1}$, using λ_{n+1} and Equation (15).

Model Verification

The composite material model was tested and verified using experimental data obtained from T800S/3900-2B [P2352W-19] BMS8-276 Rev-H-Unitape fiber/resin unidirectional composite (Ref. 21). Toray describes T800S as an intermediate modulus, high tensile strength graphite fiber. The epoxy resin system is labeled F3900 where a toughened epoxy is combined with small elastomeric particles to form a compliant interface or interleaf between fiber plies to resist impact damage and delamination (Ref. 22). Magnified views of the composite are shown in Figures 1 and 2.
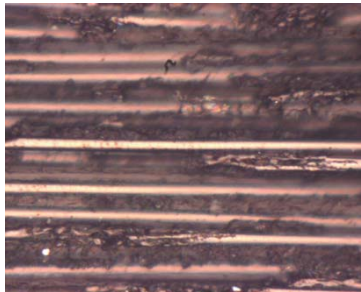
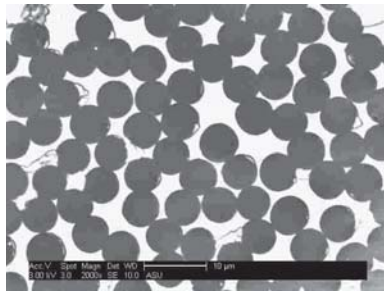Figure 1.—Side view obtained
using optical microscopy.

Figure 2.—Logitudinal view obtained
using a SEM.

The source of the input data for the model (both experimental and virtual) is listed in Table 1. In the *Data* column, *Experimental* refers to experimental data generated at Wichita State University (Ref. 21). For cases where actual experimental data were not available, numerical simulations (virtual experiments) were conducted to obtain the required stress-strain curves. To conduct the numerical experiments, micromechanics analyses were conducted where the properties of the fiber and matrix were used to simulate the response of the overall composite. Two methods were used to conduct the numerical experiments. First, the NASA GRC developed code MAC-GMC was used (Ref. 23). MAC-GMC utilized the Generalized Method of Cells to conduct a fully analytical simulation of the composite response. A second approach used a Virtual Testing Software System (Ref. 24) in which finite element models were constructed and analyzed where the fiber and matrix were explicitly modeled. For this particular unidirectional composite, as indicated in the table, due to the transverse isotropy of the material the 3-direction response was set equal to the 2-direction response. Likewise, the 1-3 shear response was set equal to the 1-2 shear response, and the off-axis response in the 1-3 plane was set equal to the off-axis response in the 1-2 plane. More details on the procedures used in the numerical experiments will be given in a future report.

The fiber (transversely isotropic, linear elastic) and the matrix (isotropic, elastic perfectly plastic) properties used in the numerical experiments are listed in Table 2. The properties for the latter are not publicly available. Hence they were correlated to obtain the values shown in the table.

The values of the coefficients in the flow rule were determined from the experimental (actual or virtual) data and the procedures outlined in Equations (3a), (3b), and (3c). The correlation curves that were used to optimize the shear coefficients in the flow law are shown in Figures 3 and 4. In the plots, the [90°] transverse tensile curve was chosen as the baseline master curve for the optimization.

TABLE 1.—GENERATION OF INPUT DATA FOR
T800-F3900 COMPOSITE

Curve	Data
Tension Test (1-Direction)	Experimental
Tension Test (2-Direction)	MAC-GMC and VTSS
Tension Test (3-Direction)	Transverse isotropy
Compression Test (1-Direction)	Experimental
Compression Test (2-Direction)	MAC-GMC and VTSS
Compression Test (3-Direction)	Transverse isotropy
Pure Shear Test (1-2 Plane)	Experimental
Pure Shear Test (2-3 Plane)	MAC-GMC and VTSS
Pure Shear Test (1-3 Plane)	Transverse isotropy
Off-Axis Test (45°, 1-2 Plane)	MAC-GMC and VTSS
Off-Axis Test (45°, 2-3 Plane)	MAC-GMC and VTSS
Off-Axis Test (45°, 1-3 Plane)	Transverse isotropy

TABLE 2.—T800-F3900 FIBER AND MATRIX PROPERTIES
(VOLUME FRACTION = 0.54)

Property	Fiber	Matrix
E_1, psi	$4(10^7)$	$5(10^5)$
E_2, psi	$2.25(10^7)$	
E_3, psi	$2.25(10^7)$	
ν_{12}	0.2	0.35
ν_{23}	0.25	
ν_{13}	0.25	
G, psi	$1.5(10^7)$	$1.85(10^5)$
σ_y, psi	----------	$2(10^4)$

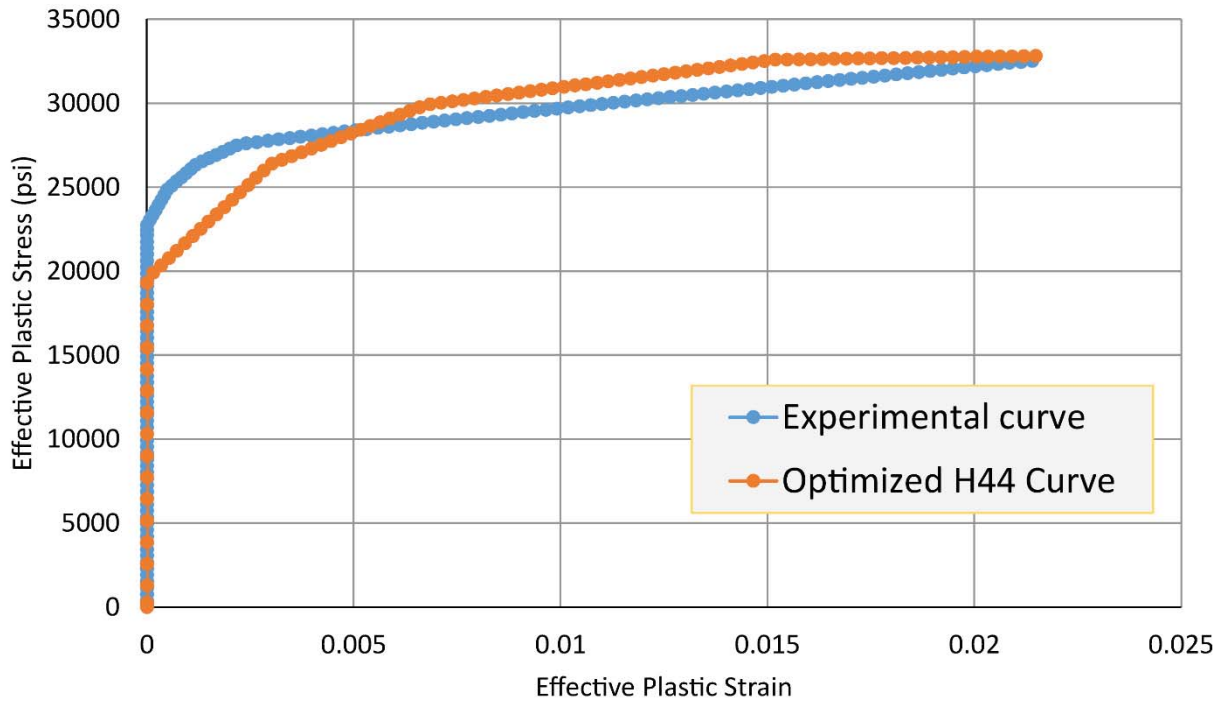# Optimized H$_{44}$ Value-Generated Curve

Figure 3.—Comparison of experimental curve with optimized H_{44} (and H_{66}) value curve.

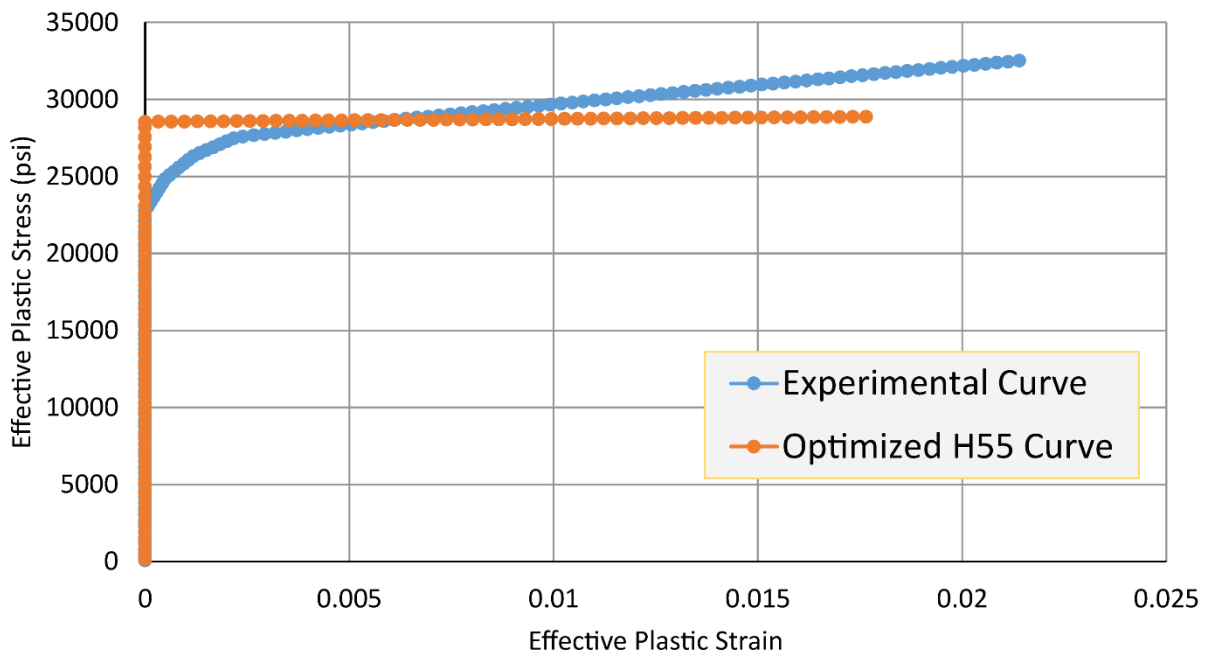# Optimized H$_{55}$ Value-Generated Curve

Figure 4.—Comparison of experimental curve with optimized H_{55} value curve.

After the determination of the required constants, the verification process was executed. In the verification test results shown in the figures that follow, the term *Experimental (Input)* refers to experimental data (when available) or to data created via virtual testing, and the term *Simulated (x-element)* refers to the data created using results from finite element simulations where *x* is the number of finite elements in the FE model.

Schematics for the tension and compression tests are shown in Figures 5 and 6, respectively. The simulations for the tension and compression tests in all three directions were executed using different mesh sizes ranging from 1 to 64 elements. The 64-element meshes for the tension and compression test cases are shown in Figures 7 and 8, respectively.
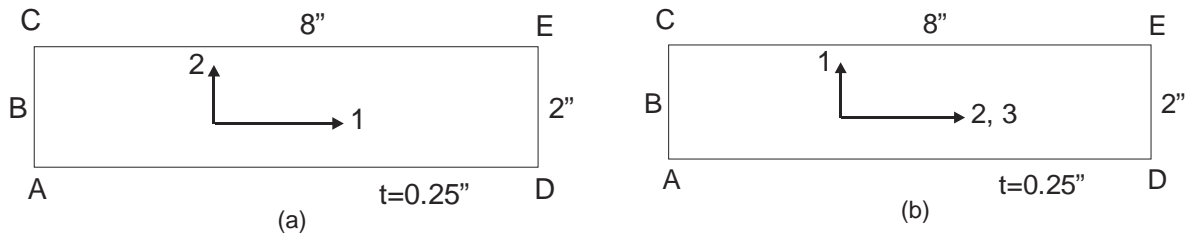
Figure 5.—Schematics for tension test simulation cases (a) 1-direction (b) 2 and 3-directions.
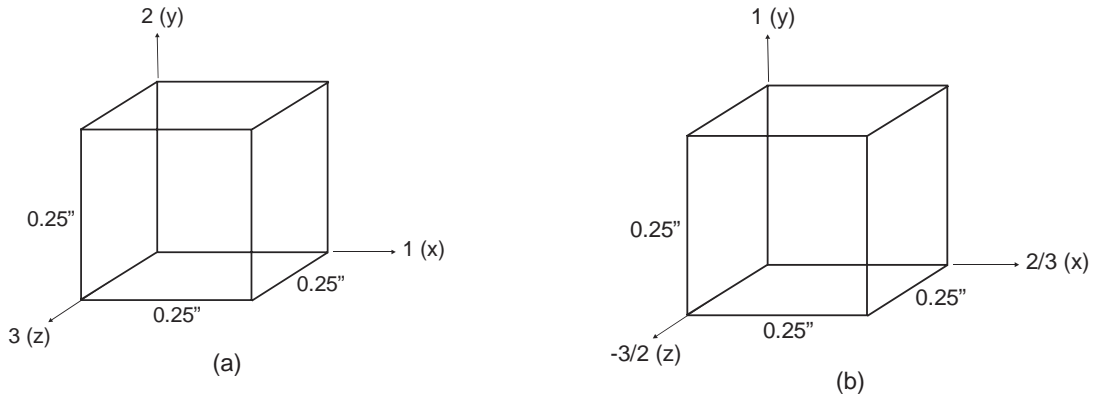
Figure 6.—Schematics for compression test simulation cases (a) 1-direction (b) 2 and 3-directions.
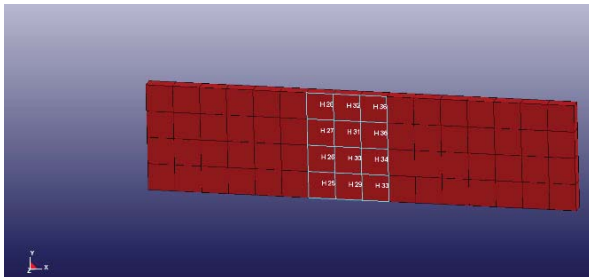
Figure 7.—The 64-element mesh for tension test cases.
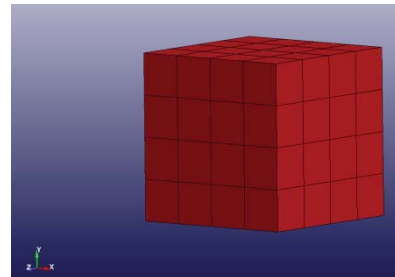
Figure 8.—The 64-element mesh for compression test cases.

For both tension and compression tests, nodes on face ABC were constrained in the x-direction and the center node was also constrained in the y-direction. A 0.5 in./s displacement in the x-direction was applied to all the nodes on the right face, E-D. For the compression tests, care was taken to ensure that the model yielded but did not buckle. The simulated and experimental stress-strain curves for the tension and compression tests are shown in Figures 9 and 10. In all cases the correlation between the input curves and the model predictions was excellent. Note that the transverse tension and compression curves (both the numerical experiments and model simulations) were artificially extended well into the nonlinear range. The extension was required in order to both fully characterize the model and to explore the capability of the model to correctly simulate the nonlinear response of the composite.

0-Degree Tension Test

(a)

0-Degree Compression Test

(b)
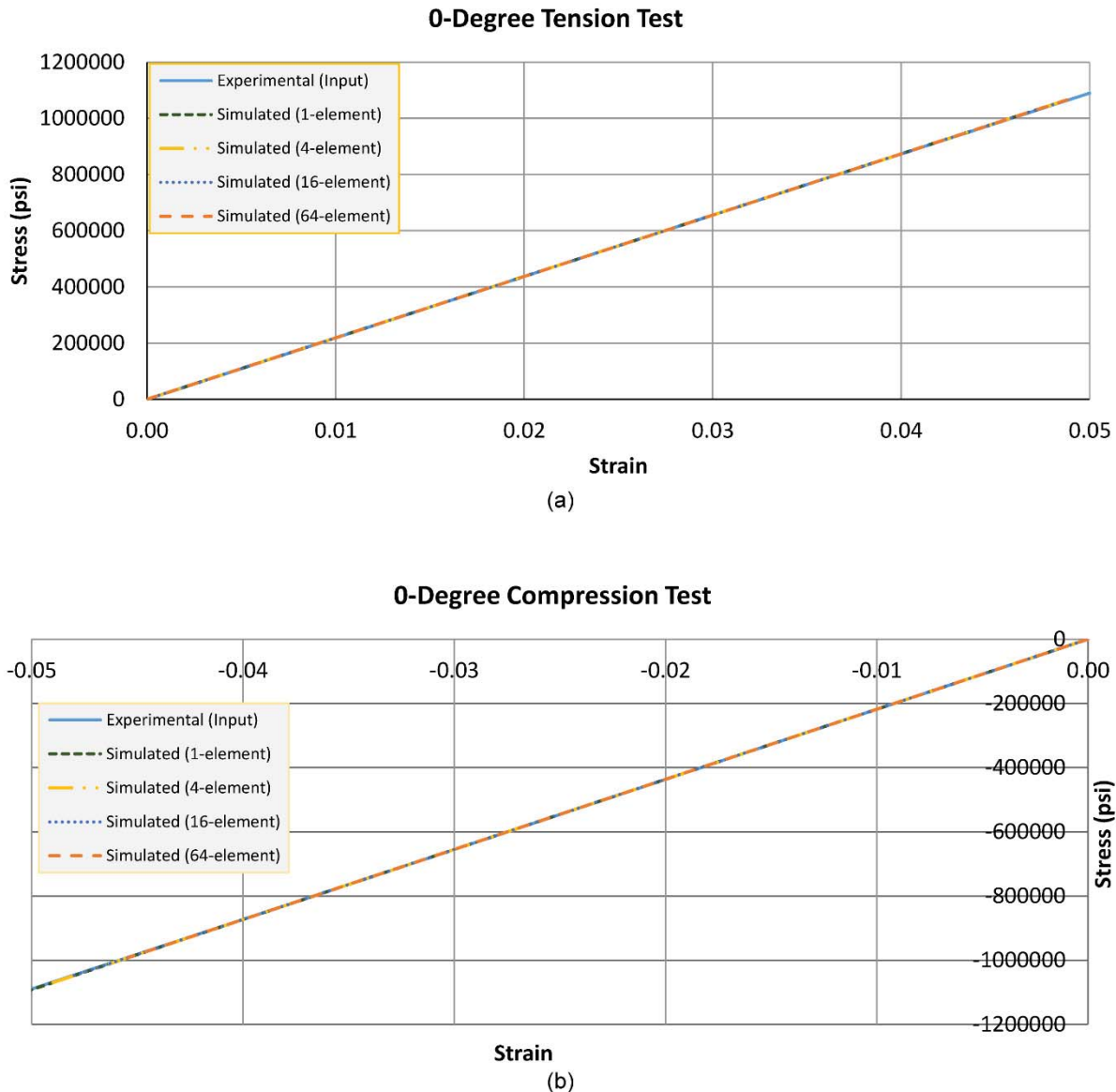
Figure 9.—Simulated and experimental stress-strain curves for 1-direction (a) tension and (b) compression.

90-Degree Tension Test (2/3-direction)

(a)

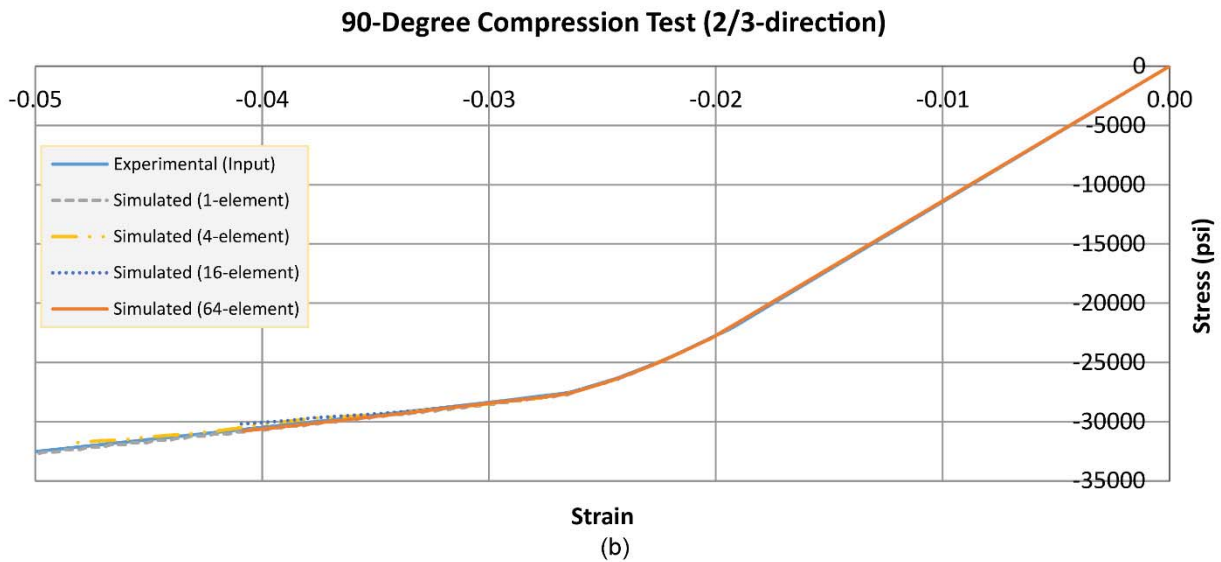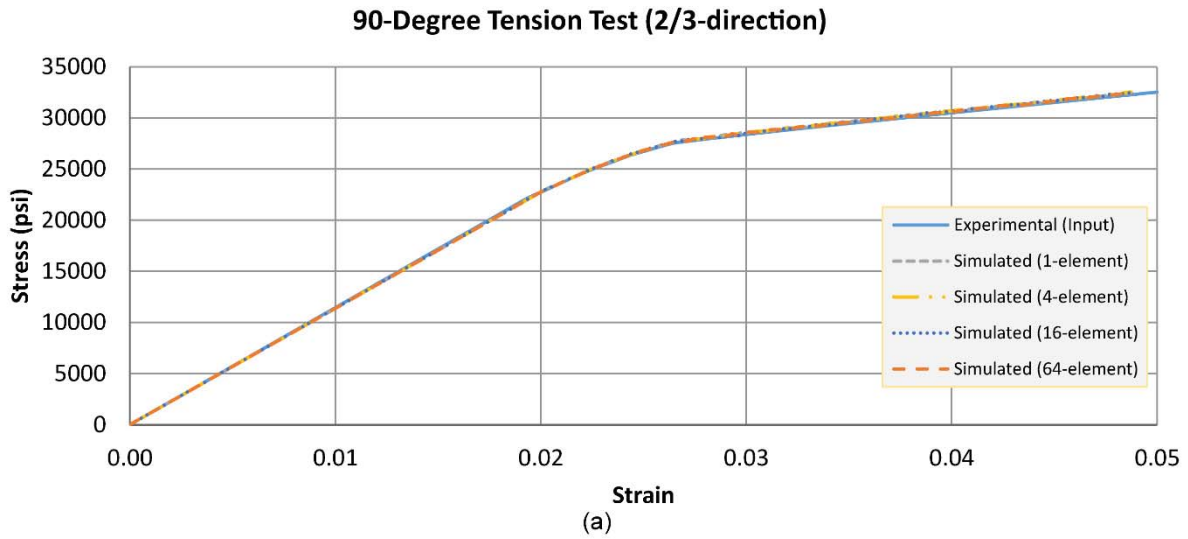## 90-Degree Compression Test (2/3-direction)

(b)

Figure 10.—Simulated and experimental stress-strain curves for 2/3-directions (a) tension and (b) compression.

A schematic for the pure shear test is shown in Figure 11. Nodes on the bottom surface are restrained in the x and y-directions while nodes on the top surface are restrained in the y-direction. A displacement controlled loading of 0.5 in./s in the x-direction is applied to all the nodes on the top surface. The 64-element mesh is shown in Figure 12. The simulated and experimental stress-strain curves in the 1-2/3-1 plane are shown in Figure 13 and in the 2-3 plane in Figure 14. Once again, the correlation between the input curves and the model predictions was excellent.

The (tension) off-axis test model in the 1-2 plane is shown in Figure 15. Nodes on face ABC were constrained in the x-direction and the center node was also constrained in the y-direction. The local element coordinate system was rotated 45° in order to simulate the off-axis response. The simulated and experimental stress-strain curves are compared in Figure 16, showing very little differences in the results, which at least partially demonstrates the ability of the model simulate the response of a composite when it is subjected to a multi-axial stress state (in the material axis system). Finally, Figure 17 shows the results from a loading-unloading-reloading test case. The model captured the results expected for a pure plasticity formulation, including a linear elastic unload with the original modulus, and a resumption of plastic flow upon reloading to the original unload point. Capturing the reduction in the unloading modulus expected for materials of this type will require the addition of a complementary damage model to the formulation.
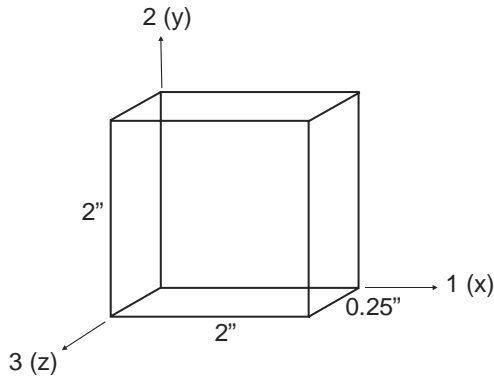

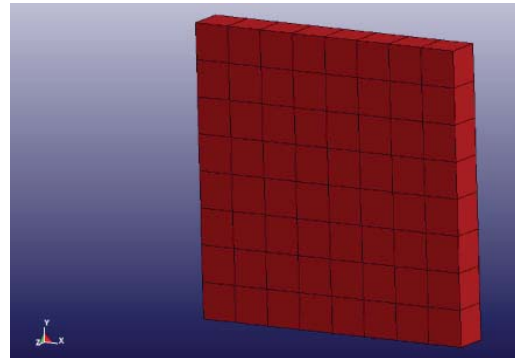Figure 11.—Schematic for pure shear test in 1-2/3-1 plane.

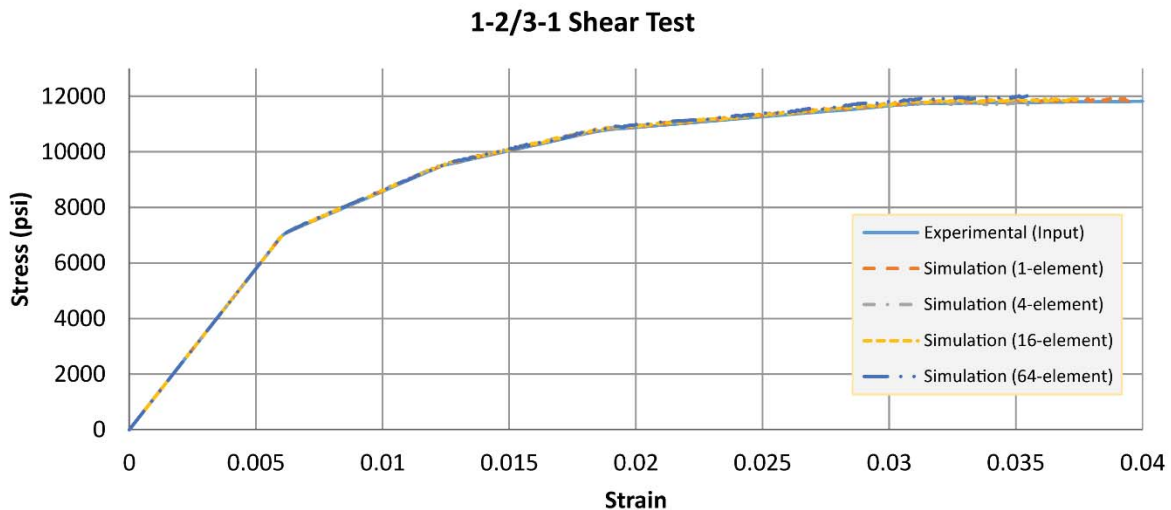Figure 12.—The 64-element mesh for pure shear test cases.

Figure 13.—Simulated and experimental stress-strain curves for pure shear in the 1-2/3-1 plane.
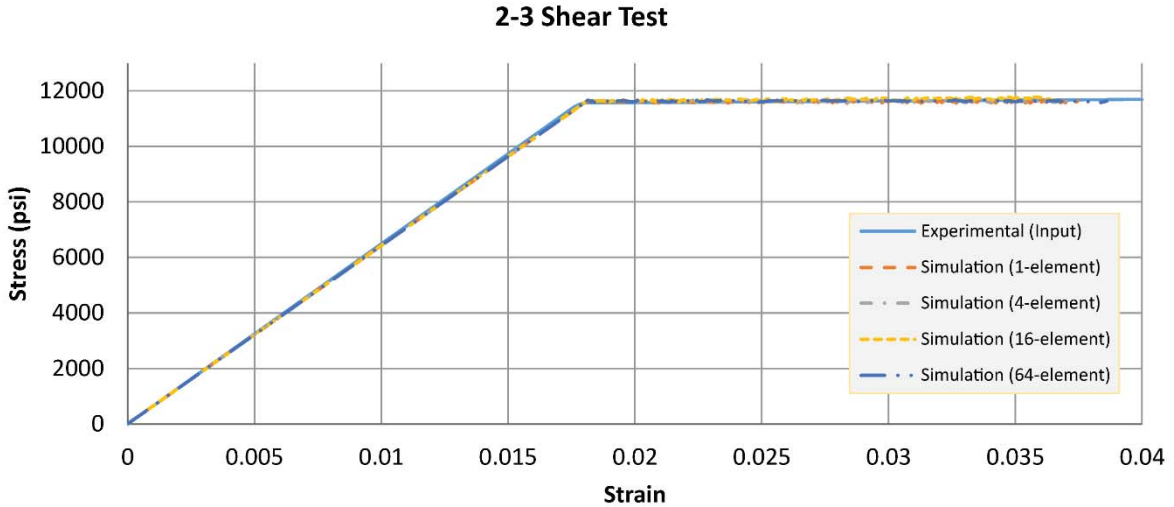
2-3 Shear Test

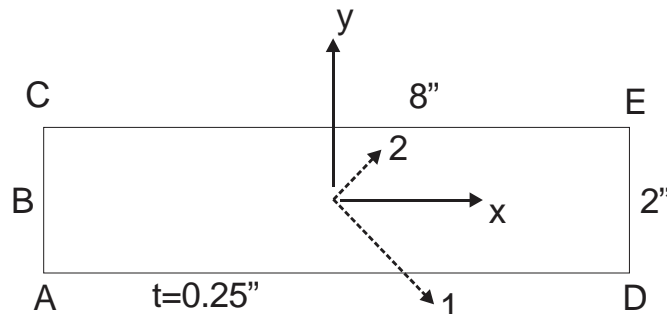Figure 14.—Simulated and experimental stress-strain curves for pure shear in the 2-3 plane.

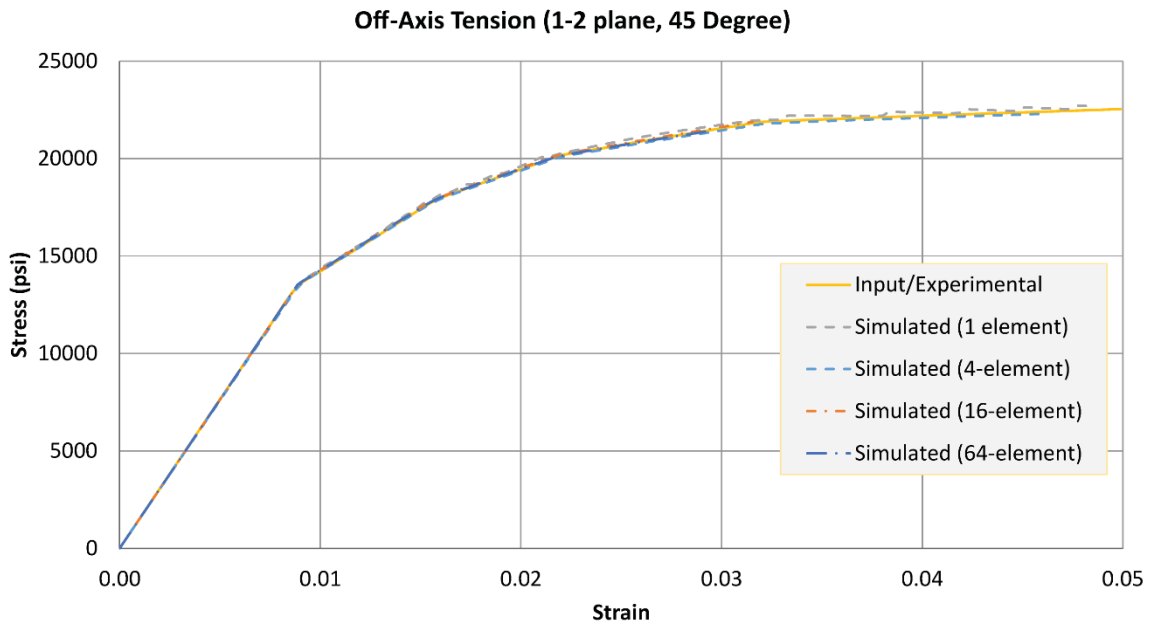Figure 15.—Schematic for 45° off axis test in 1-2/3-1 plane.

Off-Axis Tension (1-2 plane, 45 Degree)

Figure 16.—Simulated and experimental stress-strain curves for 45° off axis test in 1-2/3-1 plane.

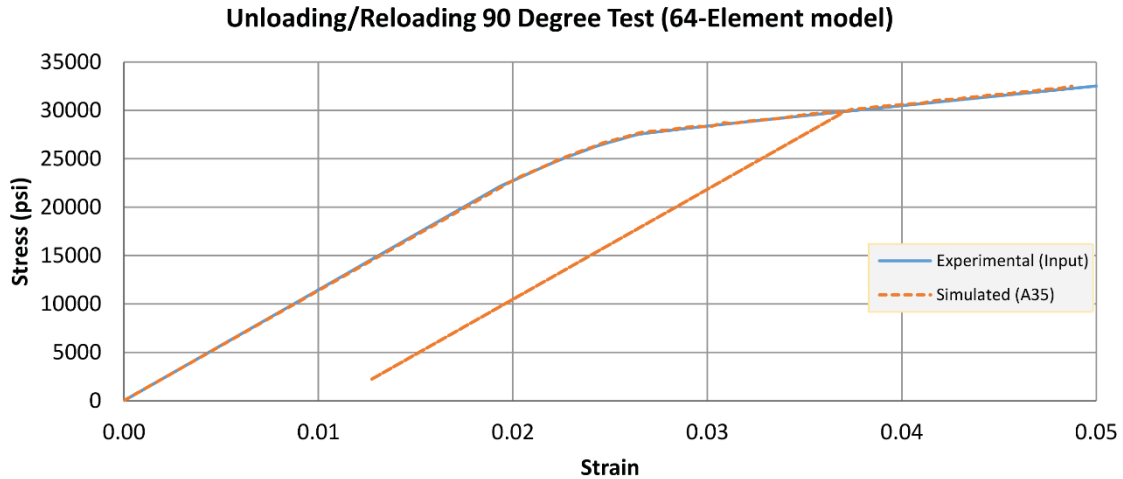**Unloading/Reloading 90 Degree Test (64-Element model)**

Figure 17.—Simulated and experimental stress-strain curves for unloading/reloading in the 2-direction.

In summary, simulations of the curves represented by the 12 input cases as an initial verification study shows very good correlation with the input data. We have used boundary conditions that resemble the experimental test setup as closely as possible so as to capture the actual test conditions. The use of four different meshes with increasing mesh density, shows that the results are mesh independent.

Structural Test

To gage the ability of the model to produce reasonable results under more realistic structural loading conditions, a structural test case was designed to qualitatively validate the developed model. A simply-supported 12 in. long by 2.4 in. wide by 0.6 in. thick plate made of T800-F3900 composite material is subjected to an impact from a steel ball. Figure 18 shows the schematic diagram. The nodes on the bottom of the left edge are constrained in the x, y and z-directions while nodes on the bottom of the right edge were constrained only in the y-direction. In the absence of experimental data, the primary objectives were to ensure that the material model (in the absence of damage and failure) would yield realistic results. That is, the ball would impact the plate and bounce back, and the peak stresses in the plate would occur around the point of contact immediately after the impact. The LS-DYNA FE model is shown in Figure 19. References to LS-DYNA keywords can be found in Hallquist (Ref. 25).

The model has 6,478 nodes and 5,707 elements of which 1,147 8-noded hexahedral elements are used to model the plate (master surface) and the remaining 4,560 elements are used in the ball (slave surface). The ball is modeled using *MAT_3 and the plate as *MAT_213. *CONTACT_AUTOMATIC_ SURFACE_TO_SURFACE is used to describe the contact between the ball and plate. Both the static (f_s) and the dynamic (f_d) coefficients of friction are set to 0.1. A 2 percent viscous damping coefficient is used. Segment-based contact is used by setting the soft parameter to 2. The steel ball is given a –700 in./s initial velocity in the y-direction. The analysis is carried out for 0.1 sec. The results are as expected. The exaggerated deformed shape is shown in Figure 20. The von Mises stress throughout the test duration is plotted for the elements closest to the point of contact in Figure 21.
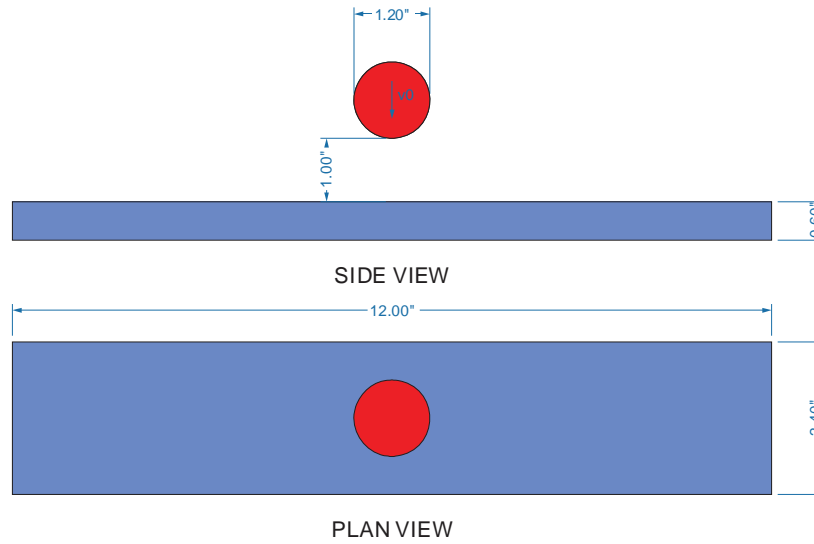
Figure 18.—Schematic diagram of the test.
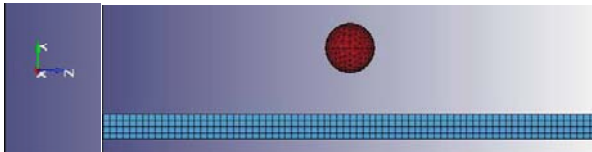

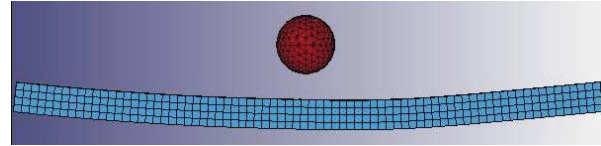Figure 19.—LS-DYNA FE model at the start of the analysis.
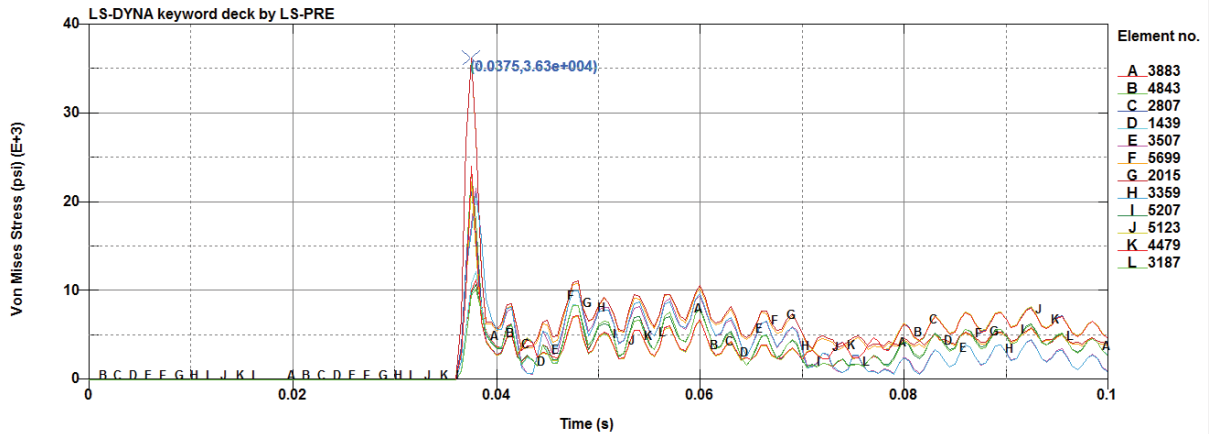

Figure 20.—Transient shape after impact.

Figure 21.—von Mises stress versus time for elements near point of impact.

Conclusions

A generalized three-dimensional composite material model is developed and verified. The preliminary results are encouraging as the implemented constitutive model is able to reproduce the experimental stress-strain curves. In addition, a simple contact problem involving the composite material yields reasonable results. Future work includes the following: adding damage accumulation and failure in the material model, supporting temperature and strain rate dependent stress-strain curves, using alternate methods to compute the plastic multiplier when the initial yield and flow surface convexity conditions are not met, using a fiber-referenced convected system to track the principal material directions and supporting plate/shell elements and to validate the developed model using data from several structural tests.

References

1. L. P. Moreira and G. Ferron, "Finite element implementation of an orthotropic plasticity model for sheet metal forming simulations," Latin American Journal of Solids and Structures, vol. 4, pp. 149-176, 2007.
2. M. Ganjiani, R. Naghdabadi and M. Asghari, "An elastoplastic damage-induced anisotropic constitutive model at finite strains," International Journal of Damage Mechanics, vol. 22, pp. 499-529, 2012.
3. J. S. Bergstrom, "Constitutive Modeling of Elastomers - Accuracy of Predictions and Numerical Efficiency," 2005. [Online]. Available: PolymerFEM.com.
4. A. Tabiei and J. Wu, "Three-dimensional nonlinear orthotropic finite element material model for wood," Composite Structures, vol. 50, pp. 143-149, 2000.
5. C. T. Sun and J. L. Chen, "A Simple Flow Rule for Characterizing Nonlinear Behavior of Fiber Composites," Journal of Composite Materials, 1989.
6. R. Vaziri, M. D. Olson and D. L. Anderson, "A Plasticity-Based Constitutive Model for Fibre-Reinforced Composite Laminates," Journal of Composite Materials, pp. 512-535, 1991.
7. G. A. Holzapfel and T. C. Gasser, "A viscoelastic model for fiber-reinforced composites at finite strains: Continuum basis, computational aspects and applications," Computer methods in applied mechanics and engineering, vol. 190, pp. 4379-4403, 2001.
8. P. B. Lourenco, R. D. Borst and J. G. Rots, "A Plane Stress Softening Plasticity Model for Orthotropic Materials," International Journal for Numerical Methods in Engineering, pp. 4033-4057, 1997.
9. Y. D. Murray and L. E. Schwer, "Verification of a general-purpose laminated composite shell element implementation: Comparisons with analytical and experimental results," Finite Elements in Analysis and Design, vol. 13, no. 1, pp. 1-16, 1993.
10. G. C. Saha and A. L. Kalamkarov, "Micromechanical Thermoelastic Model for Sandwhich Composite Shells made of Generally Orthotropic Materials," Journal of Sandwich Structures and Materials, vol. 11, pp. 27-56, 2009.
11. J. D. Littell, W. K. Binienda, W. A. Arnold, G. D. Roberts and R. K. Goldberg, "Effect of Microscopic Damage Events on Static and Ballistic Impact Strength of Triaxial Braid Composites," NASA, Washington, 2010.
12. A. Matzenmiller, J. Lubliner and R. L. Taylor, "A constitutive model for anisotropic damage in fiber-composites," Mechanics of Materials, vol. 20, pp. 125-152, 1995.
13. X. Xiao, "Modeling Energy Absorbtion with a Damage Mechanics Based Composite Material Model," Journal of Composite Materials, vol. 43, pp. 427-444, 2009.
14. F. Wu and W. Yao, "a fatigue damage model of composite materials," International Journal of Fatigue, pp. 134-138, 2010.
15. H.-S. Chen and S.-F. Hwang, "A Fatigue Damage Model for Composite Materials," Polymer Composites, pp. 301-308, 2009.

16. B. A. Gama, J.-R. Xiao, M. J. Haque, C.-F. Yen and J. W. J. Gillespie, "Experimental and Numerical Investigations on Damage and Delamination in Thick Plain Weave S-2 Glass Composites Under Quasi-Static Punch Shear Loading," U.S. Army Research Laboratory, Aberdeen Proving Ground, 2004.
17. A. F. Johnson, A. K. Pickett and P. Rozycki, "Computational methods for predicting impact damage in composite structures," Composites Science and Technology, vol. 61, pp. 2183-2192, 2001.
18. J. Ozbolt, V. Lackovic and J. Krolo, "Modeling fracture of fiber reinforced polymer," International Journal of Fracture, vol. 170, pp. 13-26, 2011.
19. C.-F. Yen, "Ballistic Impact Modeling of Composite Materials," in 7th International LS-DYNA Users Conference, 2002.
20. R. Goldberg, K. Carney, P. DuBois, C. Hoffarth, J. Harrington, S. Rajan and G. Blankenhorn, "Theoretical Development of an Orthotropic Three-Dimensional Elasto-Plastic Generalized Composite Material Model," in 13th International LS-DYNA User's Conference, Detroit, MI, 2014.
21. K. S. Raju and J. F. Acosta, "Crashworthiness of Composite Fuselage Structures - Material Dynamic Properties, Phase I," U.S. Department of Transportation: Federal Aviation Administration, Washington, DC, 2010.
22. D. L. Smith and M. B. Dow, "Properties of Three Graphite/Toughened Resin Composites," NASA Technical Paper 3102, September 1991.
23. B. A. Bednarcyk and S.M. Arnold, "MAC/GMC 4.0 User's Manual - Keywords Manual," NASA/TM—2002-212077/VOL2, National Aeronautics and Space Administration, Washington, D.C., 2002.
24. J. Harrington and S. D. Rajan, Test Results from Virtual Testing Software System, Technical Report, School of Sustainable Engineering and the Built Environment, ASU, March 2014.
25. J. Hallquist, LS-DYNA Keyword User's Manual, Version 970. Livermore Software Technology Corporation, Livermore, CA, 2013.